Data-Driven Modeling for On-Demand Flow Prescription in Fan-Array Wind Tunnels

Alejandro A. Stefan-Zavala[1*], Isabel Scherl[2], Ioannis Mandralis[1],
Steven L. Brunton[3], and Morteza Gharib[1]

[1] Graduate Aerospace Laboratories, California Institute of Technology, Pasadena, CA 91125, USA
[2] Department of Mechanical and Civil Engineering, California Institute of Technology, Pasadena, CA 91125, USA
[3] Department of Mechanical Engineering, University of Washington, Seattle, WA 98195

[*] Corresponding author. E-mail: aastefan@caltech.edu

Abstract

Fan-array wind tunnels are an emerging technology to design bespoke wind fields through grids of individually controllable fans. This design is especially suited for the turbulent, dynamic, non-uniform flow conditions found close to the ground, and has enabled applications from entomology to flight on Mars. However, due to the high dimensionality of fan-array actuation and the complexity of unsteady fluid flow, the physics of fan arrays are not fully characterized, making it difficult to prescribe arbitrary flow fields. Accessing the full capability of fan arrays requires resolving the map from time-varying grids of fan speeds to three-dimensional unsteady flow fields, which remains an open problem. This map is unfeasible to span in a single study, but it can be partitioned and studied in subsets. In this paper, we study the special case of constant fan-speeds and time-averaged streamwise velocities with one homogeneous spanwise axis. We produce a proof-of-concept surrogate model by fitting a regularized linear map to a dataset of fan-array measurements. We use this model as the basis for an open-loop control scheme to design flow profiles subject to constraints on fan speeds. In experimental validation, our model scored a mean prediction error of 1.02 m/s and our control scheme a mean tracking error of 1.05 m/s in a fan array with velocities up to 12 m/s. We empirically conclude that the physics relating constant fan speeds to time-averaged streamwise velocities are dominated by linear dynamics, and present our method as a foundational step to fully resolve fan-array wind tunnel control.

1 Introduction

Fan-array wind tunnels (i.e. fan arrays, fan walls, multi-fan wind tunnels, or Real Weather Wind Tunnels) provide an unprecedented ability to tailor fluid flows through the independent actuation of multiple fans. Compared to traditional wind tunnels with a single impeller, fan arrays have a smaller footprint for the same test-section size, have faster ramp times, and produce slower, more turbulent flows (Dougherty (2022)). The most salient feature of fan arrays is the independent actuation of each fan. Partitioning the flow source into independent units allows for spatial variation at the length-scale of one fan diameter (Dougherty (2022)). The number of achievable *static* flow profiles alone grows exponentially with the number of fans. Additionally, due to their small size and mass, each fan can change speed dynamically throughout an experiment, allowing for time-dependent flow variation.

The fan-array architecture has enabled novel wind tunnel research across a wide range of applications. Veismann et al. (2021b) used the space efficiency of fan arrays to conduct flight tests in a chamber replicating the Martian atmosphere for the *Ingenuity* Mars Helicopter. Dougherty (2022) used the independent actuation of 2,592 fans, arranged in a 3m × 3m grid, to produce compound shear layers and "checkerboard" patterns in wind, then varied fan speeds sinusoidally to perturb shear-layer vortex-shedding frequencies, in an effort to replicate "flight-relevant environments." O'Connell et al. (2022) used the same fan array, modulated sinusoidally, to produce dynamic wind conditions to develop, train and test the deep-learning autonomous flight scheme *Neural-Fly*. More examples of research leveraging fan arrays range from studies on flies (Lopez (2021)) to atmospheric turbulence (Smith et al. (2012), Ozono and Ikeda (2018) Yos et al. (2019), Veismann and Gharib (2019) Veismann and Gharib (2020), Cui et al. (2021), Veismann et al. (2021a), Walpen et al. (2023), Wei and Dabiri (2022), Mokhtar et al. (2023), Dabiri et al. (2023)); to autonomous flight on Earth (Olejnik et al. (2022), Renn (2023), Wang et al. (2021)); and on Mars (Veismann (2022), Veismann et al. (2021c)).

The breadth of successful applications of fan arrays has motivated work on their flow characterization, physics modeling, and flow prescription in recent years. Veismann et al. (2021b) determined a fan array's functional test-section (i.e. the sub-volume where turbulence intensity is minimal and boundary effects are negligible) when using only a flush-mounted honeycomb for flow conditioning. Di Luca et al. (2024a) designed multi-layered flow management devices (FMD) to improve fan-array flow quality by reducing turbulence intensity to a level seen in traditional, single-impeller wind tunnels (from 7% to 0.45%) at the cost of reduced momentum output. Dougherty (2022) showed that dual- and triple-stream free shear layers generated by fan arrays follow the same self-similarity and scaling laws as traditional "splitter plate" shear layers (Brown and Roshko (1974)). They also derived an analytical model for the free-stream velocity of an array with all fans set to the same time-varying speed. For this special case, they found that fan inertia and fluid inertia cause the fan array free-stream
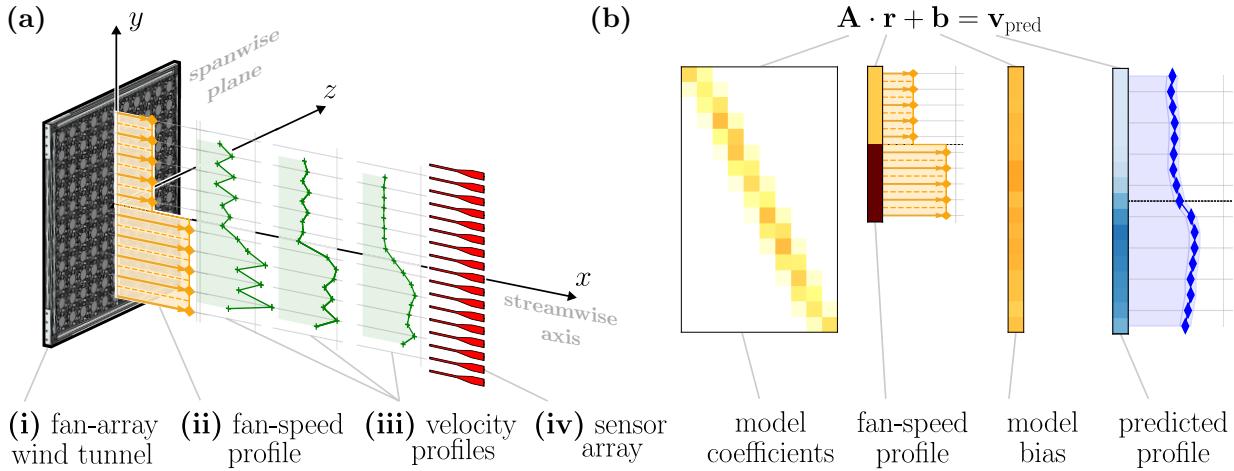
Figure 1: **(a) Left:** a fan-array wind tunnel **(i)** is given static profiles of fan speeds **(ii)** that vary along one spanwise axis (y). Mean profiles of streamwise velocity **(iii)** are measured by a sensor array **(iv)** along said axis (y). **(b) Right:** a vector of fan speeds $\mathbf{r}$ multiplied by a coefficient matrix $\mathbf{A}$, then added to a bias vector $\mathbf{b}$, gives a predicted velocity profile $\mathbf{v}_{\text{pred}}$.

flow to act as a low-pass filter of the fan-speed control signal. Di Luca et al. (2024b) derived an analytical model for the streamwise velocity of multi-plane, compound shear flows with augmented flow-conditioning. They found that this case is governed by the velocity ratio between adjacent fans, consistent with Dougherty (2022), and that their model generalizes across downstream distances when normalized by fan width. Walpen et al. (2024) used a proportional control scheme to prescribe flow conditions enabled by feedback from a motion-tracked velocimetry system. This scheme was validated by tracking a uniform flow target of 8 m/s with mean absolute errors between 0.2 and 1 m/s. Note how, across published works, fan width and total fan-array width appear as length-scales of fan-array flows.

The aforementioned studies are highlights of an actively growing body of work, each incrementally resolving fan-array physics and control. However, due to the large fan-array state space and the complexity of unsteady flow physics, designing arbitrary flows of the full available dimensionality remains an open challenge and, thus, the full capability of fan-array wind tunnels has not been achieved. To achieve this "full capability" means to prescribe both temporally and spatially varying flow fields. These flow fields can vary spatially along both spanwise axes of the fan array, at a resolution of one fan width. They can also vary temporally as fast as each fan can accelerate.

Tailoring flows in a fan array comes down to finding the right fan speeds, which can be done using a surrogate model. A surrogate model predicts the behavior of the fan array (given fan speeds, what flow is produced), and can be used to answer the inverse question: given a target flow, what fan speeds produce it. We call this process *inverse design*. An inverse-design scheme, once validated, can be used entirely without sensor feedback, freeing the fan-array test-section; or it can be used within a feedback loop to converge in less time with fewer sensors of lower resolution. A surrogate model that spans the full space of achievable temporally and spatially varying flows is infeasible to resolve in a single study, but it can be partitioned and systematically modeled in stages.

In this work, we focus on the subset of time-averaged streamwise velocity profiles produced by steady fan speeds. We couple one axis of our fan array such that all rows of fans have the same speed and only one spanwise axis is non-homogenous (our flow profiles are "one-dimensional"). See Figure 1 (a). For this special case, we produce a surrogate model and an open-loop scheme to prescribe a desired flow.

We find that a regularized linear map is an effective surrogate model for this "one-dimensional, static" fan-array case. This linear map is encoded as a coefficient matrix and a bias vector, shown in Figure 1 (b). The resulting model coefficients match intuition: each velocity reading is primarily affected by the fan-row directly upstream of it, secondarily affected by adjacent fan-rows, and insensitive to distant fan-rows. Fitting models on profiles measured further away from the source appears to capture the effect of viscous diffusion and turbulent mixing, visible as a "smearing" of model coefficients (shown in Figure 5).

We apply this model as the basis of a linear program to find the best fan speeds for desired velocity profiles via inverse design. The linear program can be constrained on both fan speeds and predicted velocity profile. These constraints are critical in practice, where noise restrictions, power limitations, and fan-unit failure can impose new requirements on the state-space in which a model was trained. We experimentally validate both out-of-sample prediction and open-loop tracking performance using inputs and targets produced after fitting.

This paper is structured as follows: In Section 2 we describe our fan array (2.1.1), sensors (2.1.2), mathematics (2.2), and datasets (2.3); in Section 3 we present the model coefficients (3.1), prediction performance (3.2), and tracking performance (3.3) obtained in validation experiments; Section 4 contains concluding remarks and considerations for future research towards complete fan-array modeling and control.
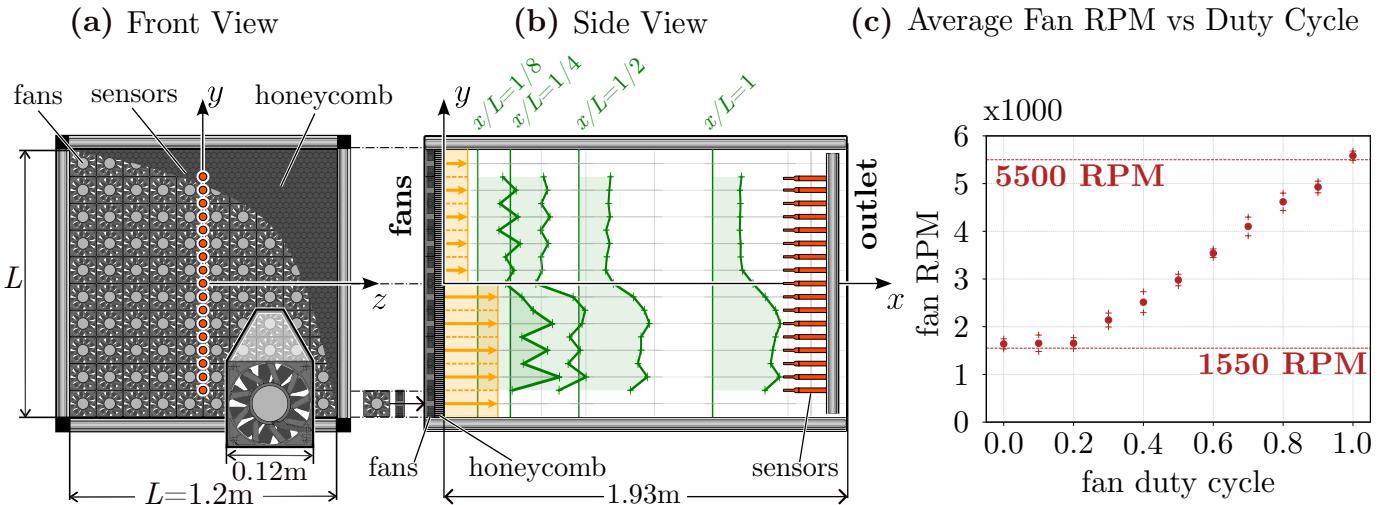
(a) Front View   **(b)** Side View   **(c)** Average Fan RPM vs Duty Cycle

Figure 2: Experimental setup. **(a)** Front view of 10×10 fan array, showing the alignment of each sensor in orange circles along the middle of the array. **(b)** Fan-array side view, with example velocity profiles at each of the four downstream distances measured. The sensor array is traversed along the x axis. **(c)** average RPM versus duty-cycle for all fans.

2 Methods

2.1 Experimental Design

2.1.1 Fan Array Wind Tunnel

The model and control method presented in this paper are built entirely on experimentally collected fan array data. There are three signals in a fan array flow experiment: (1) the control signal to each fan, (2) the speed (rotational rate) of each fan and (3) the flow measured at some downstream location. Fan control signals are encoded as Pulse-Width Modulation (PWM) *duty-cycle*, which ranges from 0 or 0% (lowest fan speed) to 1 or 100% (highest fan speed). Fan speed is measured in revolutions per minute (RPM). Flow is measured in its streamwise component (x), is averaged in time, and is normalized by a reference velocity $V_{\max} = 11$ m/s.

We use a 10×10-fan array, composed of 100 DELTA PFC1212DE-F00 120mm $\times$ 120mm fan units. This array spans a square 1.22m $\times$ 1.22m (spanwise) enclosed open-loop test section that extends 1.93m downstream. See Figure 2 (a)-(b). For this fan unit, the mapping from duty cycle to RPM is linear from 20% duty cycle (nominally $1,550$ RPM) to 100% duty cycle (nominally $5,500$ RPM). For duty cycles below 20% these fans remain at their RPM floor of $1,550$ RPM. We use one flush-mounted 6.35mm diameter, 38.1mm thick "honeycomb" for flow conditioning. We normalize coordinates in the test section by the width of the fan array, $L = 1.2$m. This is the same fan-array wind tunnel as used by Cossé et al. (2014), Sader et al. (2016) and Fan et al. (2019).

To control our fan array, we partition it into five 2×10 "modules," each spanning two rows of the full 10×10 grid. Each module has one NUCLEO F429ZI microcontroller, which directly controls and monitors each of its 20 fans. All five microcontrollers are coordinated by a desktop computer over a Local Area Network. Our fan-array control software is available open-source (Stefan-Zavala (2023)).

2.1.2 Sensor Array

We use an array of 17 Sensirion SDP31 digital differential pressure sensors arranged along the spanwise axis (y) and centered in the middle of our fan array. The 17 sensors are aligned with the centers and edges of fans. (Figure 2 **(a)-(b)**). The sensor array is traversed along the streamwise axis (x), such that profiles are measured at different downstream distances within the $z = 0$ plane. The pressure sensors are placed in a 3D-printed housing and used as pitot-tube anemometers to measure streamwise velocity. All sensors are queried serially through the I2C serial protocol using an Adafruit TCA9548A multiplexer. A Teensy 4.0 microcontroller queries the full sensor array at 9.2 Hz. For a given fan-speed profile, data was collected for 7 seconds then averaged in time. Sensor readings are averaged in time and, at $x/L = 1$, have standard deviations ranging from 0.06 m/s to 1.8 m/s, with an average standard deviation of 0.31 m/s. Our data collection and processing scripts are implemented using Jupyter Notebook 7.0 (Kluyver et al. (2016)) and the Python 3.11.3 kernel, as well as numpy version 1.26.4 (Harris et al. (2020)), pandas version 2.2.1 (McKinney (2010)), and Matplotlib version 3.8.4.

(a) Surrogate Model

```python
from sklearn.linear_model \
    import Lasso
# R.shape == (N_fans,N_data)
# V.shape == (N_sensors,N_data)
LS = Lasso(alpha=0.01)
LS.fit(R.T, V.T)
A = LS.coef_
b = LS.intercept_
# use: v_hat = A@r + b
#
# r.shape == (N_fans,)
# v.shape == (N_sensors,)
```

(b) Inverse Design

```python
from scipy.optimize \
    import least_squares
# v_star.shape==(N_sensors,)
f = lambda r: (A@r+b)-v_star
# lb, ub are min,max fan dc
lb = np.zeros((N_fans,))
ub = np.ones((N_fans,))
r0 = np.random.rand(N_fans)
result = least_squares(f,r0,
    bounds=(lb, ub),
    loss='soft_l1')
r_hat = result.x
```

Figure 3: Implementation of mathematical methods in Python 3. **(a)** Regression of surrogate model given input dataset $\mathbf{R}$ and output dataset $\mathbf{V}$. **(b)** Inverse-design application of the surrogate model to estimate the best input $\hat{\mathbf{r}}$ for a desired profile $\mathbf{v}_{\text{target}}$.

2.1.3 Functional Test-Section: Fan Array Boundary Effects

There are three key boundary effects for the test-section of a fan array: close to the array, far from the array, and at the spanwise edges of the array. These effects are studied in detail by Veismann et al. (2021b) and Dougherty (2022). When close to the fans (small x/L), the effect of fan geometry (such as the size of a fan's hub and the boundary between each fan) is observable in the flow profile. With increasing distance from the fans (increasing x/L), artifacts from fan geometry are dampened by viscous diffusion and turbulent mixing. Diffusion and mixing, however, also dampen variations due to nonuniform fan speeds, the essential feature of fan arrays. Measuring too close to the fan array introduces artifacts, measuring too far negates individual-fan control. For the fan array used in this paper, we found $x/L = 1$ to be a good downstream distance based on this trade-off.

At the spanwise edges of the fan array ($|y/L|$ and $|z/L|$ close to $1/2$), a boundary layer will form with the test-section enclosure (or a free-shear layer in the case of an open test-section). Veismann et al. (2021b) recommends $y/L, z/L \in [-0.4, 0.4]$. The span of our sensor array in this paper matches this recommendation.

2.2 Mathematical Methods

2.2.1 Surrogate Model

Let $\mathbf{r} = [r_1,\ r_2,\ ... r_{N_{\text{fans}}}]$ be a fan-speed profile. The component r_j is the duty cycle of the jth actuator, and is a real-valued scalar ranging from 0 (lowest fan speed) to 1 (maximum fan speed). Since we couple each row of fans in our 10×10 array to the same duty cycle, we have $N_{\text{fans}} = 10$ actuators and r_j is the jth *row* of fans (Figure 2 (a)). We say $\mathbf{r}$ is an input into the fan array.

Let $\mathbf{v} = [v_1,\ v_2,\ ... v_{N_{\text{sensors}}}]$ be a velocity profile at a fixed downstream distance. The component v_i is the nondimensionalized, time-averaged, streamwise velocity reading of the ith sensor in an array of N_{sensors} sensors, and is a real-valued positive scalar. In this paper, we have $N_{\text{sensors}} = 17$ sensors along the nonhomogeneous spanwise axis y (Figure 2 (b)). We say $\mathbf{v}$ is an output of the fan array. A fan-array surrogate model predicts the output $\mathbf{v}$ produced by a given input .

Let N be the number of all experimentally collected profiles at a given downstream distance, each consisting of an input-output pair $(\mathbf{r}, \mathbf{v})$. Let $\mathbf{R} \in \mathbb{R}^{n \times N}$ be the matrix of N horizontally stacked input vectors and $\mathbf{v} \in \mathbb{V}^{m \times N}$ be the matrix of N horizontally stacked output vectors,

$$\mathbf{R} = \begin{bmatrix} | & | & | & & | \\ \mathbf{r}_1 & \mathbf{r}_2 & \mathbf{r}_3 & ... & \mathbf{r}_N \\ | & | & | & & | \end{bmatrix} \quad \mathbf{V} = \begin{bmatrix} | & | & | & & | \\ \mathbf{v}_1 & \mathbf{v}_2 & \mathbf{v}_3 & ... & \mathbf{v}_N \\ | & | & | & & | \end{bmatrix}.$$

Our surrogate model consists of an $m \times n$ coefficient matrix $\mathbf{A}$ and an m-dimensional bias vector $\mathbf{b}$. Given an input , an estimate $\mathbf{v}_{\text{pred}}$ of the true output $\mathbf{v}$ is given by

$$\mathbf{v}_{\text{pred}} = \mathbf{A}\mathbf{r} + \mathbf{b}.$$

We produce our surrogate model $(\mathbf{A}, \mathbf{b})$ from our data matrices $\mathbf{R}$ and $\mathbf{v}$ using regularized linear regression. This means we find the $\mathbf{A}$ and $\mathbf{b}$ that best map $\mathbf{R}$ to $\mathbf{v}$ such that $\mathbf{A}\mathbf{R} + \mathbf{b} \approx \mathbf{v}$. This is the same as minimizing the l_2 norm $||\mathbf{A}\mathbf{R} + \mathbf{b} - \mathbf{v}||_2$. To regularize, we penalize the l_1 norm (the sum of coefficient magnitudes) of $\mathbf{A}$ and $\mathbf{b}$. The explicit form of our regression is
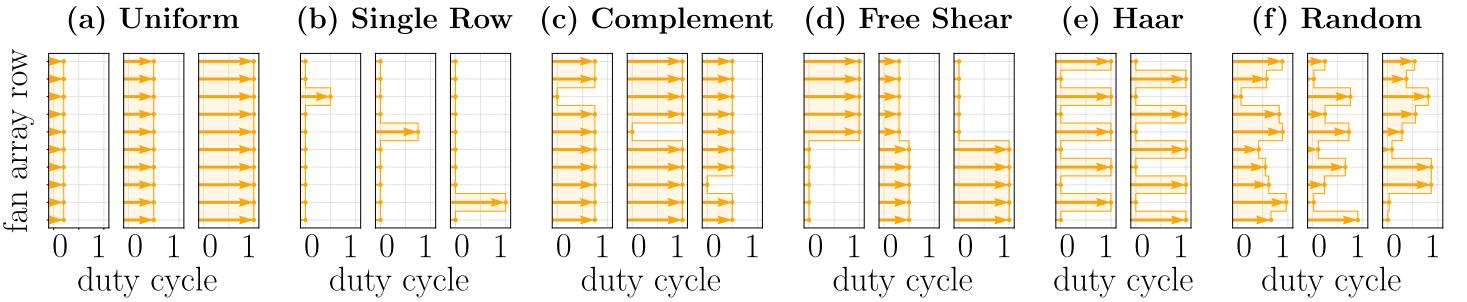
Figure 4: Types of inputs used in data collection. **(a) Uniform**: all fans to the same duty cycle. **(b) Single Row:** one fan-row at nonzero duty-cycle, all other fans at zero duty-cycle. **(c) Complement:** one fan-row at zero duty-cycle, all others at nonzero duty-cycle. **(d) Free Shear:** top half and bottom half of the fan array at different duty cycles. **(e) Haar:** Concatenated Haar wavelets at different resolutions, and their mirror profiles. **(f) Random:** each fan-row at a random duty-cycle, sampled from a uniform distribution.

$$\mathbf{A}, \mathbf{b} = \underset{\mathbf{A},\mathbf{b}}{\operatorname{argmin}} \quad \frac{1}{2N_{\text{data}}} ||\mathbf{AR} + \mathbf{b} - \mathbf{V}||_2^2 + \alpha(||\mathbf{A}||_1 + ||\mathbf{b}||_1).$$

For our final model, we chose a regularization parameter $\alpha = 0.01$. Our implementation in code is given in Figure 3 (a). It is built on Scikit-learn 1.5.1 (Pedregosa et al. (2011)).

Linear regression regularized by the l_1 norm is known as LASSO regression. Regularizing on the l_1 norm promotes model sparsity, which is a proxy for simplicity. The effect of regularization on our model is discussed in Section 3.1.

2.2.2   Inverse Design

Given a desired flow profile $\mathbf{v}_{\text{target}}$, we use our surrogate model $(\mathbf{A}, \mathbf{b})$ to find the input $\hat{\mathbf{r}}$ that produces the closest profile to $\mathbf{v}_{\text{target}}$:

$$\hat{\mathbf{r}} = \min_{\mathbf{r}} ||\mathbf{Ar} + \mathbf{b} - \mathbf{v}_{\text{target}}||_2$$

subject to

$$l_k \leq r_k \leq u_k$$

where l_k and u_k are lower and upper bounds on the duty-cycle of each fan. Use them to encode limitations on fan speed, such as saturation ($l_k = 0, u_k = 1$) or 'dead' fans ($l_k = u_k = 0$). Our implementation in code is given in Figure 3 (b). It is built on SciPy 1.12.0 (Virtanen et al. (2020)).

2.3   Data Description

To fit our models, we start with a set $\mathbf{R}_{\text{train}}$ of 169 inputs. For each input, we measure the output profile at four downstream distances: $x/L = 1/8$, $x/L = 1/4$, $x/L = 1/2$ and $x/L = 1$, using the setup described in Section 2.1. For each downstream distance, we compile a set $\mathbf{V}_{\text{train}}$ of 169 measured outputs corresponding to $\mathbf{R}_{\text{train}}$. For each pair $(\mathbf{R}_{\text{train}}, \mathbf{V}_{\text{train}})$ we fit a surrogate model $(\mathbf{A},)$ as described in Section 2.2.1.

The inputs that form set $\mathbf{R}_{\text{train}}$ fall within six "types" of profiles, described in Figure 4. These profile types were chosen for their relevance in previous fan-array experiments (Uniform and Free-Shear), their potential use as basis for the fan-array input space (Single-Row and Complement), and for broad coverage of the input space (Haar and Random). The 169 profiles of the training set break down into types as follows: 11 Uniform, 60 Single-Row, 40 Complement, 10 Free Shear, 8 Haar, and 40 Random. The resulting models are shown and described in Section 3.1.

To validate our model predictions, we use a set $\mathbf{R}_{\text{test}}$ of 63 inputs. Test inputs are of the same profile types as training inputs, but with different parameters and duty-cycles. At each modeled downstream distance a set of predicted profiles $\hat{\mathbf{V}}_{\text{test}}$ is compared against a set of measured profiles $\mathbf{V}_{\text{test}}$. Prediction performance is described in Section 3.2

We validate the tracking performance of our inverse-design scheme using a set of 34 target *output* profiles (not inputs). Tracking performance is described in Section 3.3
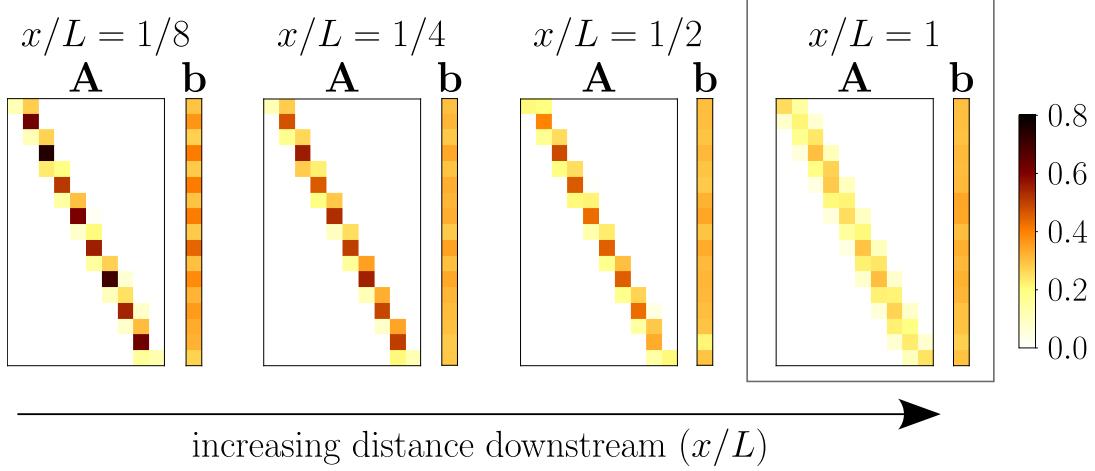
Figure 5: Resulting model coefficient matrices ($\mathbf{A}$) and bias vectors ($\mathbf{b}$). As x/L increases, model coefficients appear to "diffuse." To the right, highlighted, $x/L = 1$ is the preferred distance for the fan array modeled in this study.

3   Results

3.1   Surrogate Model

The surrogate model ($\mathbf{A}, \mathbf{b}$) (Section 2.2.1) was fit to map between training dataset pairs ($\mathbf{R}, \mathbf{v}$) at the four measured locations $x/L \in \{1/8, 1/4, 1/2, 1\}$ (Section 2.3). The resulting model coefficients and biases are shown in Figure 5. According to the model coefficients, each sensor reading (row of $\mathbf{A}$) is primarily affected by the speed of fans (columns of $\mathbf{A}$) directly upstream, secondarily affected by adjacent fans, and insensitive to all other fans. This is encoded by the tri-diagonal-like structure of $\mathbf{A}$. Comparing model coefficients as x/L increases shows effects that may be attributed to turbulent mixing and viscous diffusion as flow structures advect downstream. That is, the influence of each fan mixes with that of neighboring fans: As x/L increases, model coefficients become less sparse, smaller in magnitude, and more similar. The influence of fan geometry is evident when the coefficients for sensors aligned with fan *hubs* are different from those aligned with fan *edges*. This is the case for all measured x/L *less than* 1. where coefficients at fan hubs (near 0.6 for $x/L = 1/8$) are up to three times larger than coefficients for fan edges (near 0.2 for $x/L = 1/8$). At $x/L = 1$, the coefficients at fan hubs and fan edges are most similar, ranging from 0.1 to 0.25. Therefore, at $x/L = 1$ the effect of fan geometry is small, while custom velocity profiles are still achievable. It is from this trade-off between velocity profile smoothness and controllability that $x/L = 1$ is the preferred downstream distance for this fan array (Section 2.1.3). Bias vectors $\mathbf{b}$ (Section 2.2.1) capture the fixed nonzero fan RPM for duty cycles at or below 0.3 specific to this fan array (Section 2.1.1, Figure 2 (**c**)), which results in a fixed velocity "floor" of $0.3V_{\max}$ or 0.34 m/s at $x/L = 1$.

The further away we measure from the source, the more linear the map between fan and velocity profiles appears to be, and therefore the better our models fit. Similarly, the average R^2 value across all 17 output variables is lowest at $x/L = 1/8$ with $R^2 = 0.74$, highest at $x/L = 1/2$ with $R^2 = 0.81$, and is $R^2 = 0.79$ at $x/L = 1$. These R^2 values suggest most of the variation in sensor readings is explained by the linear fits, and moreso with increasing x/L.

3.2   Output Prediction

Out-of-sample (not seen in training) performance was tested with predictions for 63 brand new fan array inputs versus their measured "true" velocity profiles at each x/L. We quantify *prediction error* as mean absolute error (MAE) between measured and predicted profiles. For a *single* input $\mathbf{r}$, prediction $\mathbf{v}_{\mathrm{pred}} = \mathbf{A}\mathbf{r} + \mathbf{b}$ and true measurement $\mathbf{v}_{\mathrm{true}}$, the prediction error of this one sample is the average absolute value of the component-wise difference between $\mathbf{v}_{\mathrm{true}} - \mathbf{v}_{\mathrm{pred}}$:

$$\mathrm{MAE}(\mathbf{v}_{\mathrm{true}}, \mathbf{v}_{\mathrm{pred}}) = \frac{1}{N_{\mathrm{sensors}}} \sum_{k}^{N_{\mathrm{sensors}}} |v_k - \hat{v}_k| \qquad \begin{aligned} \mathbf{v}_{\mathrm{true}} &= [v_1, v_2, ... v_k, ... v_{N_{\mathrm{sensors}}}]^{\mathrm{T}} \\ \mathbf{v}_{\mathrm{pred}} &= [\hat{v}_1, \hat{v}_2, ... \hat{v}_k, ... \hat{v}_{N_{\mathrm{sensors}}}]^{\mathrm{T}} \end{aligned} \qquad (1)$$

The prediction error for an entire dataset is the average of all sample-wise MAEs. Since our profiles are normalized by $V_{\max} = 11$ m/s, this MAE is in nondimensional velocity as a fraction of $V_{\max}$. Multiplying by $V_{\max}$ gives the dimensional MAE's reported in this section.

At the preferred downstream distance $x/L = 1$, testing MAE is 0.093 $v_{\mathrm{error}}/V_{\max}$ or 1.02 m/s and training MAE is 0.057 $v_{\mathrm{error}}/V_{\max}$ or 0.63 m/s. This performance is consistent across downstream distances: The additional distances $x/L \in$
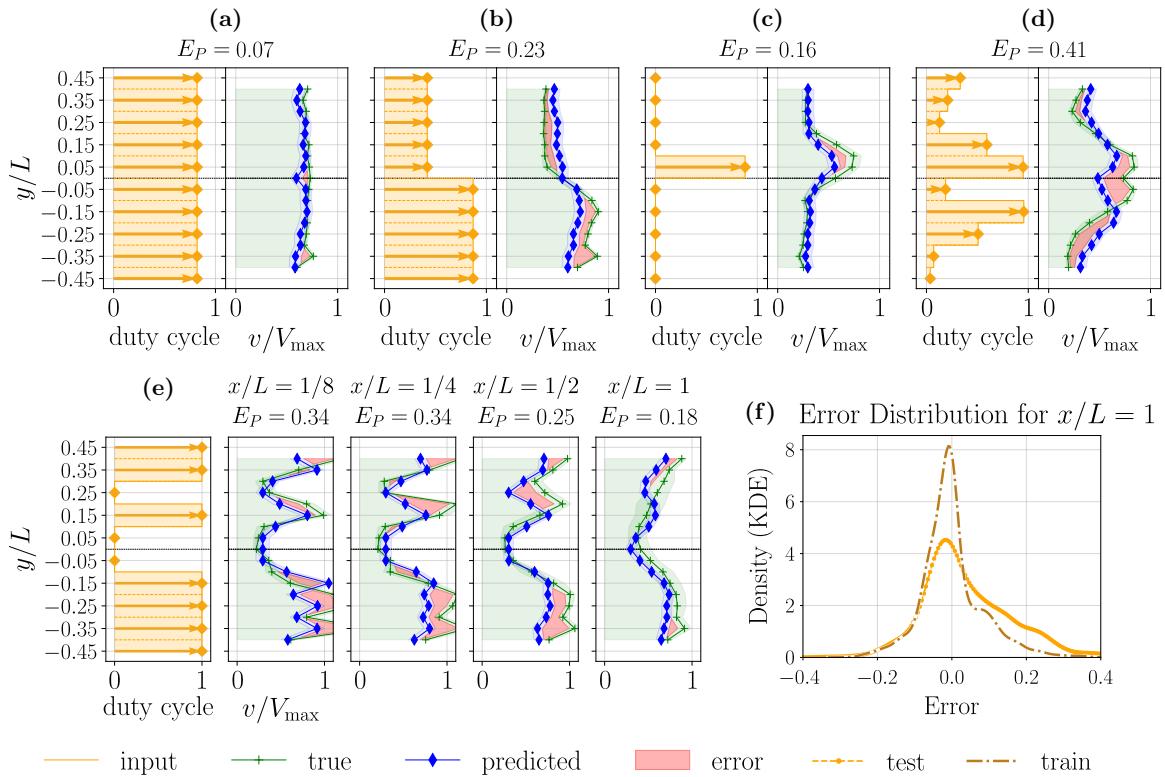
Figure 6: **Top.** Example profiles from test-set at $x/L = 1$, showing input profile, model prediction and true measurement. **Bottom. Left:** Example test-set profiles at all modeled downstream distances. **Right:** Kernel-Density plots showing the distribution of component-wise (signed) prediction errors $(v - \hat{v})$ for both train and test set. Sample-wise mean absolute percent error (MAPE) E_P is shown above each sample.

$\{1/2, 1/4, 1/8\}$ have dimensional testing MAE's of 1.04 m/s, 1.06 m/s and 1.16 m/s, respectively, and dimensional training MAE's of 0.61 m/s, 0.72 m/s and 0.86 m/s, respectively. This gives an average out-of-sample (test-set) prediction error of 1.07 m/s across all measured x/L.

We additionally compute mean absolute percentage error (MAPE), which normalizes the component-wise error by the absolute value of the $\mathbf{v}_{\text{true}}$ component:

$$\text{MAPE}(\mathbf{v}_{\text{true}}, \mathbf{v}_{\text{pred}}) = \frac{1}{N_{\text{sensors}}} \sum_{k}^{N_{\text{sensors}}} \frac{|v_k - \hat{v}_k|}{\max(|v_k|, \epsilon)} \quad \begin{aligned} \mathbf{v}_{\text{true}} &= [v_1, v_2, ...v_k, ...v_{N_{\text{sensors}}}]^{\text{T}} \\ \mathbf{v}_{\text{pred}} &= [\hat{v}_1, \hat{v}_2, ...\hat{v}_k, ...\hat{v}_{N_{\text{sensors}}}]^{\text{T}} \end{aligned} \quad (2)$$

ϵ is an arbitrary, small constant used to prevent division by zero. At the preferred downstream distance $x/L = 1$, training and testing MAPE's are 0.132 (13%) and 0.173 (17.3%), respectively. The additional distances, $x/L \in \{1/8, 1/4, 1/2\}$ have training MAPE's of 0.158, 0.146, 0.126, and testing MAPE's of 0.186, 0.176, 0.164, respectively. The MAPE's of individual samples are shown in Figure 6. MAE and MAPE are calculated using the Scikit-learn 1.5.1 implementations `mean_absolute_error` and `mean_absolute_percentage_error`, respectively (Pedregosa et al. (2011)).

Kernel-density plots of signed, component-wise error distributions $(v_{\text{true}} - v_{\text{pred}})$ at $x/L = 1$, shown in Figure 6 **(f)**, show a bias towards positive error or undershooting $(v_{\text{pred}} < v_{\text{true}})$, stronger in testing than in training. This pattern is observable in all samples shown in Figure 6 **(a)-(e)**, where most errors (red shade) consist of measured profiles (green crosses) being larger (to the right) of predicted profiles (blue diamonds). We attribute most error to nonlinear fluid dynamic effects, which a linear map of unmodified input features cannot capture.

3.3 Inverse Design

Tracking performance of the inverse-design open-loop control algorithm described in Section 2.2.2 was tested at the preferred downstream distance $x/L = 1$ using a set of 34 target velocity profiles not present in testing or training datasets.

We quantify *tracking error* the same way as prediction error in Section 3.2, as mean absolute error between a *target* velocity profile $\mathbf{v}_{\text{target}}$ and the *measured* velocity profile $\mathbf{v}_{\text{measured}}$ that results from executing the fan array input $\mathbf{r}$ produced by the inverse-design algorithm to track $\mathbf{v}_{\text{target}}$, the tracking error of a single sample is given by $\text{MAE}(\mathbf{v}_{\text{target}}, \mathbf{v}_{\text{measured}})$ in 1. The tracking error of the entire inverse-design test-dataset is the average of all sample-wise tracking errors. The $x/L = 1$
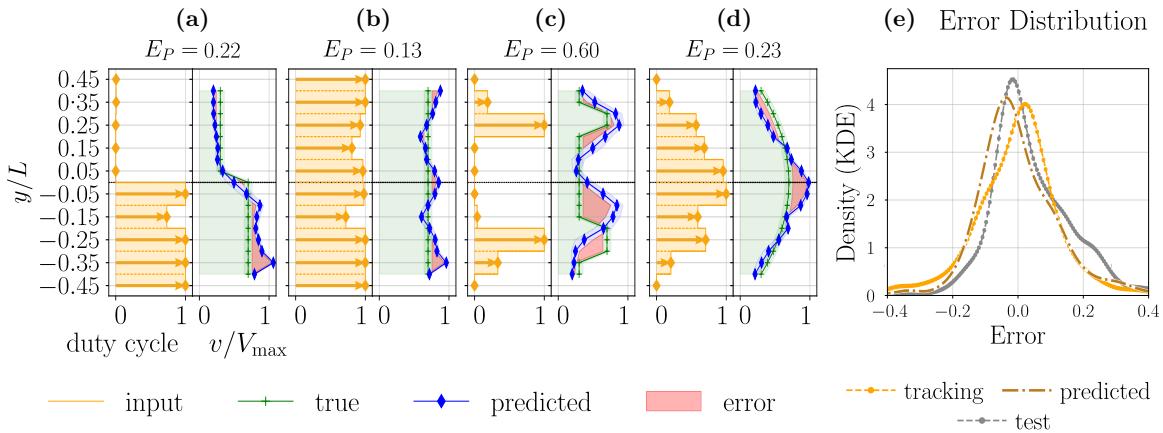
Figure 7: Example profiles from inverse-design validation at $x/L = 1$, showing resulting control input (yellow), target flow (green) and true measurement (blue). **Rightmost:** Kernel-Density plot of the distribution of (signed) component-wise tracking error ($v_{\text{target}} - v$), along with prediction error *for inverse-design inputs*, and prediction test-error from Figure 6. Sample-wise mean absolute percent error (MAPE) E_P is shown above each sample.

inverse-design test-set has a normalized MAE of 0.095 $v_{\text{error}}/V_{\text{max}}$ and a MAPE of 0.215. This gives an average dimensional tracking error of 1.05 m/s for $x/L = 1$. Test-set prediction MAE for $x/L = 1$ is 1.02 m/s (Section 3.2). MAE suggests the inverse-design open-loop control algorithm is as effective at tracking target profiles as the underlying linear model is at predicting profiles, if slightly worse at lower velocities, as suggested by higher MAPE. This consistency in performance between tracking and prediction is visible in Figure 7 **(e)**.

Comparing the distribution of signed tracking errors in Figure 7 **(e)** shows complementary biases: prediction error is biased towards underestimating outputs and tracking error is, in turn, biased towards overshooting targets. The profiles in Figure 7 **(a)-(d)** show this overshooting, where measured profiles (blue diamonds) are most often of larger magnitude (to the right) of target profiles (green crosses). Additionally, as is the case with prediction error, the dominant source of error appears to be nonlinear fluid-dynamic effects, most evident in Figure 7 **(c)-(d)**.

4 Conclusion

The key feature of fan arrays is the independent control of multiple flow sources. Space efficiency, rapid speed-modulation and characteristic turbulence are also distinguishing, useful features worthy of study. However, independent control of each impeller is the feature that sets fan arrays apart as a potential field of study of their own: the field of replicating arbitrary fluid-flows by finding suitable fan speeds. This fine control is also the feature with the most complexity and unanswered questions. At its full richness, using a fan array means prescribing a three-component, unsteady turbulent velocity field in a three-dimensional volume, as a function of time-varying grids.

In this work, we modeled the steady-state, streamwise velocity profiles of an array of coupled rows of fans, as a function of fan duty-cycle. In search of the simplest model that works, we used l_1-regularized linear regression to encode steady-state fan array physics as a sparse coefficient matrix and a bias vector. The parsimony of our design resulted in a model that is not only simple and effective, but also interpretable. The matrix coefficients show an intuitive relation between sensors and actuators. Comparing the model fit at different downstream distances shows the effect of viscous diffusion and turbulent mixing (Figure 5). We successfully applied and validated this model, both to predict the output of out-of-sample fan-array inputs and to find desired velocity profiles subject to constraints on fan speeds. Though restricted to a special case, our model covers a large and vastly applicable range of fluid flows. Steady-state streamwise velocity profiles that vary along one axis are a large swath of classical fluid dynamics. We can now prescribe shear layers without splitter plates and Couette flows without moving walls, and we can change shear ratios and forcing velocities without modifying the test section. We can even prescribe some unsteadiness. For example, although the profile of a shear layer is steady, the Kelvin-Helmholtz instability at its core has rich turbulent dynamics which are a function of the steady-state profile (Dougherty (2022)). Finally, the open-loop nature of our inverse-design scheme allows for flow prescription without a sensor array occupying the test section, where one typically places the object of study in an experiment.

One avenue for future work in this area is to better resolve the model under the present assumptions. In this work, our model was fit from fan duty-cycles to flow velocities. Though there is a linear relation between fan duty-cycle and RPM (Figure 2-**(c)**), fitting a map from RPM to flow velocity captures the underlying physics more directly than from duty-cycle to flow velocity. Duty-cycle is the control signal into a fan, while RPM is the actual rotational speed of the fan. Fans of the same model have slight variations in RPM for the same duty cycle. A fan that is blocked, damaged or worn out will also have its RPM response affected. A map from RPM to flow velocity will hold true even as fan units deteriorate, are perturbed,

or are replaced. Though only one spanwise direction was resolved, we hypothesize that our exact method (Section 2.2.1), can be applied to a setting with both spanwise axes actuated (i.e. fan-rows decoupled and the full fan-array is controllable). Our inverse-design scheme is effective without feedback. However, this model can also be used as the basis for closed-loop control. A feedback control scheme would compensate for unmodeled dynamics, a dominant source of error in Sections 3.2 and 3.3. Looking at the coefficient matrices in Section 3.1 suggests an underlying smooth kernel, which is superimposed at the time of prediction. The alternating magnitudes of coefficients with fan hubs and fan edges resembles superimposing Gaussian profiles centered at each fan. Finding this kernel may enable a resolution-invariant, self-similar representation of the fan array, where prediction is done by convolving this kernel with a curve of fan speeds. As shown in Section 3.1, our linear fit captured most of the underlying pattern in our training data, with an R^2 value around 0.8 across all datasets. The remaining unmodeled dynamics can be captured by adding nonlinear input features. The added model complexity can be kept minimal with regularization that promotes sparsity, such as the present l_1 regularization, or with a more sophisticated method that enables a large library of candidate nonlinearities (Brunton et al. (2016)).

Another direction for continued research is to relax simplifying assumptions and model new regimes of fan-array dynamics. One such extension is time-resolved fan-array flows. Modeling flows from inputs that both vary in time (e.g. varying fan-speeds in sine waves as done by Ozono and Ikeda (2018) and Dougherty (2022)) and are resolved along a spanwise axis, would enable the prescription of arbitrary unsteady flow profiles. A similar approach can be used for frequency content. The modes of a flow can be added as input features and modeled as a function of fan speeds, which makes flow power spectrum prescribable. Controlling power spectrum would allow for power-spectra matching of flows measured in nature, and for tailored studies of frequency response in experiments. Another two dimensions to model are the spanwise components of the velocity field. In fan arrays where all fan outlets point in the same direction, flow will be dominated by its streamwise component. Still, there exist applications in which spanwise velocities are critical, such as spanwise gusts that perturb autonomous fliers from the side or from below.

As shown in Figure 5, there is a clear pattern of diffusion and smearing in model coefficients with increasing distance downstream. If this diffusion effect is modeled, one can obtain coefficients for all locations in the test section despite having only measured at a few streamwise locations. Finally, a large enough body of work would allow for the map from fan specifications and array configuration to the surrogate model that would be obtained from such a design. Predicting what surrogate model will be obtained by a fan-array enables the highest abstraction of inverse-design: given the flows you wish to make, what fan array should you build and how should you control it. This would attain the most general and resolved level of fan-array modeling and control. With this capability, any gust, breeze, plume or tide, from anywhere on Earth or Mars, can be replicated, faithfully, in lab, as can all the phenomena of Nature and engineering that fly, swim, float or exist therein.

Declaration of Interests The authors declare no conflict of interest.

Author Contributions conceptualization: A.S.Z., S.L.B., I.M.; data collection – proof-of-concept: A.S.Z., I.M.; data collection – for publication: A.S.Z., I.S.; formal analysis: A.S.Z., I.S., S.L.B.; visualization: A.S.Z., I.S., S.L.B.; funding acquisition: M.G.; supervision: I.S., S.L.B., M.G.; writing – original draft: A.S.Z; writing – review and editing: A.S.Z., I.S., S.L.B., I.M.

Data Availability Statement Raw data are available from the corresponding author A.S.Z., upon reasonable request.

Ethical Standards The research meets all ethical guidelines, including adherence to the legal requirements of the study country.

Supplementary Material Code supplement available at `https://github.com/astefanz/fml-1`.

References

Brown, G. L. and Roshko, A. (1974). On density effects and large structure in turbulent mixing layers. *Journal of Fluid Mechanics*, 64(4):775–816.

Brunton, S. L., Proctor, J. L., and Kutz, J. N. (2016). Discovering governing equations from data by sparse identification of nonlinear dynamical systems. *Proceedings of the National Academy of Sciences*, 113(15):3932–3937. Publisher: Proceedings of the National Academy of Sciences.

Cossé, J., Sader, J., Kim, D., Cerdeira, C. H., and Gharib, M. (2014). The Effect of Aspect Ratio and Angle of Attack on the Transition Regions of the Inverted Flag Instability. American Society of Mechanical Engineers Digital Collection.

Cui, W., Zhao, L., Cao, S., and Ge, Y. (2021). Generating unconventional wind flow in an actively controlled multi-fan wind tunnel. *Wind and Structures*, 33(2):115–122. Number: 2.

Dabiri, J. O., Howland, M. F., Fu, M. K., and Goldshmid, R. H. (2023). Visual anemometry for physics-informed inference of wind. *Nature Reviews Physics*, 5(10):597–611. Publisher: Nature Publishing Group.

Di Luca, M., Leipold, M., and Noca, F. (2024a). Design, implementation and validation of a flow management device for fan-array wind tunnels. In *AIAA SCITECH 2024 Forum*. American Institute of Aeronautics and Astronautics. _eprint: https://arc.aiaa.org/doi/pdf/10.2514/6.2024-2673.

Di Luca, M., Leipold, M., and Noca, F. (2024b). On the generation of plane compound shear flows with fan-array wind tunnels. In *AIAA SCITECH 2024 Forum*. American Institute of Aeronautics and Astronautics. _eprint: https://arc.aiaa.org/doi/pdf/10.2514/6.2024-2672.

Dougherty, C. J. (2022). *On the Experimental Simulation of Atmospheric-Like Disturbances Near the Surface*. phd, California Institute of Technology.

Fan, B., Huertas-Cerdeira, C., Cossé, J., Sader, J. E., and Gharib, M. (2019). Effect of morphology on the large-amplitude flapping dynamics of an inverted flag in a uniform flow. *Journal of Fluid Mechanics*, 874:526–547. Publisher: Cambridge University Press.

Harris, C. R., Millman, K. J., van der Walt, S. J., Gommers, R., Virtanen, P., Cournapeau, D., Wieser, E., Taylor, J., Berg, S., Smith, N. J., Kern, R., Picus, M., Hoyer, S., van Kerkwijk, M. H., Brett, M., Haldane, A., del Río, J. F., Wiebe, M., Peterson, P., Gérard-Marchant, P., Sheppard, K., Reddy, T., Weckesser, W., Abbasi, H., Gohlke, C., and Oliphant, T. E. (2020). Array programming with NumPy. *Nature*, 585(7825):357–362. Publisher: Nature Publishing Group.

Hunter, J. D. (2007). Matplotlib: A 2D Graphics Environment. *Computing in Science & Engineering*, 9(3):90–95. Conference Name: Computing in Science & Engineering.

Kluyver, T., Ragan-Kelley, B., Pérez, F., Bussonnier, M., Frederic, J., Hamrick, J., Grout, J., Corlay, S., Ivanov, P., Abdalla, S., and Willing, C. (2016). Jupyter Notebooks—a publishing format for reproducible computational workflows.

Lopez, A. (2021). Characterization of fluid flow inside a multi-fan-array wind tunnel for insects. page F20.002. Conference Name: APS Division of Fluid Dynamics Meeting Abstracts ADS Bibcode: 2021APS..DFDF20002L.

McKinney, W. (2010). Data Structures for Statistical Computing in Python. *Proceedings of the 9th Python in Science Conference*, pages 56–61. Conference Name: Proceedings of the 9th Python in Science Conference.

Mokhtar, N. O., Fernández-Cabán, P. L., and Catarelli, R. A. (2023). Automated large-scale and terrain-induced turbulence modulation of atmospheric surface layer flows in a large wind tunnel. *Experiments in Fluids*, 65(1):5.

O'Connell, M., Shi, G., Shi, X., Azizzadenesheli, K., Anandkumar, A., Yue, Y., and Chung, S.-J. (2022). Neural-Fly enables rapid learning for agile flight in strong winds | Science Robotics.

Olejnik, D. A., Wang, S., Dupeyroux, J., Stroobants, S., Karasek, M., De Wagter, C., and de Croon, G. (2022). An Experimental Study of Wind Resistance and Power Consumption in MAVs with a Low-Speed Multi-Fan Wind System. In *2022 International Conference on Robotics and Automation (ICRA)*, pages 2989–2994.

Ozono, S. and Ikeda, H. (2018). Realization of both high-intensity and large-scale turbulence using a multi-fan wind tunnel. *Experiments in Fluids*, 59(12):187.

Pedregosa, F., Varoquaux, G., Gramfort, A., Michel, V., Thirion, B., Grisel, O., Blondel, M., Prettenhofer, P., Weiss, R., Dubourg, V., Vanderplas, J., Passos, A., Cournapeau, D., Brucher, M., Perrot, M., and Duchesnay, A. (2011). Scikit-learn: Machine Learning in Python. *Journal of Machine Learning Research*, 12(85):2825–2830.

Renn, P. I. J. (2023). *Applied Machine Learning for Prediction and Control of Fluid Flows*. phd, California Institute of Technology.

Sader, J. E., Huertas-Cerdeira, C., and Gharib, M. (2016). Stability of slender inverted flags and rods in uniform steady flow. *Journal of Fluid Mechanics*, 809:873–894.

Smith, J. T., Masters, F. J., Liu, Z., and Reinhold, T. A. (2012). A simplified approach to simulate prescribed boundary layer flow conditions in a multiple controlled fan wind tunnel. *Journal of Wind Engineering and Industrial Aerodynamics*, 109:79–88.

Stefan-Zavala, A. A. (2023). https://github.com/astefanz/fan-club. original-date: 2023-05-10T18:48:59Z.

Veismann, M. (2022). *Axial Descent of Multirotor Configurations – Experimental Studies for Terrestrial and Extraterrestrial Applications.* phd, California Institute of Technology.

Veismann, M., Burdick, J., Gharib, M., Wei, S., Conley, S., Young, L., Delaune, J., and Izraelevitz, J. (2021a). Axial Descent of Variable-Pitch Multirotor Configurations: An Experimental and Computational Study for Mars Deployment Applications. The Vertical Flight Society.

Veismann, M., Dougherty, C., Rabinovitch, J., Quon, A., and Gharib, M. (2021b). Low-density multi-fan wind tunnel design and testing for the Ingenuity Mars Helicopter. *Experiments in Fluids*, 62(9):193.

Veismann, M. and Gharib, M. (2019). Characterization of Rotor-Rotor Aerodynamic Interactions for Free Flight Studies of Multirotor Systems. page B17.003. Conference Name: APS Division of Fluid Dynamics Meeting Abstracts ADS Bibcode: 2019APS..DFDB17003V.

Veismann, M. and Gharib, M. (2020). High Fidelity Aerodynamic Force Estimation for Multirotor Crafts in Free Flight. In *AIAA Scitech 2020 Forum*, AIAA SciTech Forum. American Institute of Aeronautics and Astronautics.

Veismann, M., Wei, S., Conley, S., Young, L., Delaune, J., Burdick, J., Gharib, M., and Izraelevitz, J. (2021c). Axial Descent of Variable-Pitch Multirotor Configurations: An Experimental Investigation under Free-Flight Settings for Mars Deployment Applications. page P25.002. Conference Name: APS Division of Fluid Dynamics Meeting Abstracts ADS Bibcode: 2021APS..DFDP25002V.

Virtanen, P., Gommers, R., Oliphant, T. E., Haberland, M., Reddy, T., Cournapeau, D., Burovski, E., Peterson, P., Weckesser, W., Bright, J., van der Walt, S. J., Brett, M., Wilson, J., Millman, K. J., Mayorov, N., Nelson, A. R. J., Jones, E., Kern, R., Larson, E., Carey, C. J., Polat, A., Feng, Y., Moore, E. W., VanderPlas, J., Laxalde, D., Perktold, J., Cimrman, R., Henriksen, I., Quintero, E. A., Harris, C. R., Archibald, A. M., Ribeiro, A. H., Pedregosa, F., and van Mulbregt, P. (2020). SciPy 1.0: fundamental algorithms for scientific computing in Python. *Nature Methods*, 17(3):261–272. Publisher: Nature Publishing Group.

Walpen, A., Catry, G., and Noca, F. (2023). Real-Scale Atmospheric Wind and Turbulence Replication using a Fan-Array for Environmental Testing and UAV/AAM Validation. In *AIAA SCITECH 2023 Forum*. American Institute of Aeronautics and Astronautics. _eprint: https://arc.aiaa.org/doi/pdf/10.2514/6.2023-0812.

Walpen, A., Govoni, T., Stirnemann, J., Ionescu, M., Bosson, N., Catry, G., and Noca, F. (2024). Automated control of complex aerodynamic flows generated by Windshaper fan arrays. In *AIAA SCITECH 2024 Forum*, AIAA SciTech Forum. American Institute of Aeronautics and Astronautics.

Wang, N., Kjellberg, C. W. R., Catry, G., Bosson, N., Sanyal, A., and Glauser, M. (2021). Turbulent flows generated by fan array wind tunnel. page F20.003. Conference Name: APS Division of Fluid Dynamics Meeting Abstracts ADS Bibcode: 2021APS..DFDF20003W.

Wei, N. J. and Dabiri, J. O. (2022). Phase-averaged dynamics of a periodically surging wind turbine. *Journal of Renewable and Sustainable Energy*, 14(1):013305.

Yos, D., Gharib, M., and Veismann, M. (2019). Improving the Descent Performance of Small-Scale Rotorcraft through Added Geometries. page NP05.048. Conference Name: APS Division of Fluid Dynamics Meeting Abstracts ADS Bibcode: 2019APS..DFDN05048Y.